Editors' Suggestion   Featured in Physics

Giant momentum-dependent spin splitting in centrosymmetric low-*Z* antiferromagnets

Lin-Ding Yuan,[1] Zhi Wang,[1,*] Jun-Wei Luo,[2] Emmanuel I. Rashba ●,[3,†] and Alex Zunger[1,‡]

[1]*Energy Institute, University of Colorado, Boulder, Colorado 80309, USA*
[2]*State Key Laboratory for Superlattices and Microstructures, Institute of Semiconductors,*
Chinese Academy of Sciences, Beijing 100083, China
[3]*Department of Physics, Harvard University, Cambridge, Massachusetts 02138, USA*

The energy vs crystal momentum $E(k)$ diagram for a solid (band structure) constitutes the road map for navigating its optical, magnetic, and transport properties. By selecting crystals with specific atom types, composition, and symmetries, one could design a target band structure and thus desired properties. A particularly attractive outcome would be to design energy bands that are split into spin components with a momentum-dependent splitting, as envisioned by Pekar and Rashba [Zh. Eksp. Teor. Fiz. **47**, 1927 (1964)], enabling spintronic application. The current paper provides "design principles" for wave-vector dependent spin splitting (SS) of energy bands that parallel the traditional Dresselhaus and Rashba spin-orbit coupling (SOC)–induced splitting, but originates from a fundamentally different source—antiferromagnetism. We identify a few generic antiferromagnetic (AFM) prototypes with distinct SS patterns using magnetic symmetry design principles. These tools allow also the identification of specific AFM compounds with SS belonging to different prototypes. A specific compound—centrosymmetric tetragonal MnF_2—is used via density functional band-structure calculations to quantitatively illustrate one type of AFM SS. Unlike the traditional SOC-induced effects restricted to noncentrosymmetric crystals, we show that antiferromagnetic-induced spin splitting broadens the playing field to include even centrosymmetric compounds, and gives SS comparable in magnitude to the best known ("giant"' SOC effects, even without traditional SOC, and consequently does not rely on the often-unstable high atomic number elements required for high SOC. We envision that use of the current design principles to identify an optimal antiferromagnet with spin-split energy bands would be beneficial for efficient spin-charge conversion and spin-orbit torque applications without the burden of requiring compounds containing heavy elements.

I. INTRODUCTION

An electron with momentum p and mass m moving in an inversion symmetry-breaking electric field E in a solid experiences an effective magnetic field $B_{\mathrm{eff}} \sim E \times p/mc^2$ in its rest frame, where c is the speed of light. In bulk crystals [1] this symmetry-breaking electric field is given by the gradient of the crystal potential $E = -\nabla V$, whereas in heterostructures [2] it can be produced by interfacial asymmetry, and in centrosymmetric compounds by the local asymmetry of individual structural sectors [3]. This intrinsic magnetic field couples the electron momentum to its spin, a relativistic effect leading to spin-orbit-coupling (SOC)–induced spin splitting of energy bands at wave vectors differing from the time-reversal invariant moments (TRIM). In the semirelativistic Pauli equation, the SOC is described by the Thomas (T) [4] term $H_{\mathrm{T}} = -\frac{e\hbar}{4m^2c^2}\{\sigma \cdot [\nabla V(\mathbf{r}) \times \mathbf{p}]\}$ that couples electron spin σ to its coordinate r and momentum p, and it's fully relativistic generalization. These seminal studies have formed the basis for the development of spintronics [5–7], bringing k-dependent spin-orbit interaction to the forefront of solid-state

physics, including applications to spin transistor, spin-orbit torque, spin Hall effect, topological insulators, and Majorana Fermions (see the review in Ref. [8]).

Since the relativistic SOC increases rapidly with atomic number Z, and since the strength of chemical bonds in compounds decreases rapidly with increasing atomic number (e.g., in the sequence ZnTe-CdTe-HgTe, or ZnS-ZnSe-ZnTe [9]), the ease of breaking such fragile high-Z bonds—creating vacancies that produce free carriers—has been an unwelcome but constant companion of high SOC compounds both for spin splitting and for topological insulators applications [9–12]. This double limitation of the Rashba and Dresselhaus [1,2] spin splitting effects to high-Z and noncentrosymmetric compounds has limited the playing field, raising hopes for an alternative spin splitting mechanism in thermodynamically stable, low-Z compounds of more general symmetries.

More recently, the investigation of spin splitting of energy bands has been expanded to magnetic systems, in particular, antiferromagnets, for eliminating stray fields [13–16]. For example, spin splitting has been calculated in some high-Z AFM half-metallic compounds such as iron-pnictide AFM $BaCrFeAs_2$ [17], Mn_3Al and Mn_3Ga [18], and two-dimensional (2D) van der Waals [19] AFM materials, but such occurrences were not distinct from the traditional spin-orbit effect [1,2]. Indeed, it is generally implied that such splitting in the presence of background antiferromagnets may

*Corresponding author: zhi.wang@colorado.edu
†erashba@physics.harvard.edu
‡Corresponding author: alex.zunger@colorado.edu

be treated just as SOC-induced splitting in nonmagnetic (NM) materials [1,2], through the usual Thomas term [4], for example, allowing for antiferromagnetism in calculations on $BiCoO_3$ [20] having SOC manifests but a small change in its spin splitting; furthermore, if SOC is deliberately removed from the Hamiltonian, the predicted spin splitting vanishes in the whole Brillouin zone (BZ). Also, the field-free magnetic mechanism discussed in the present paper differs from the anomalous spin-orbit coupling in antiferromagnets induced by applying external magnetic field, discussed in Refs. [21,22].

A phenomenological theory of magnetic spin splitting was proposed in 1964 by Pekar and Rashba [23], suggesting that the presence in magnetic compounds of a spatially dependent intrinsic magnetic field $\mathbf{h}(\mathbf{r})$, periodic with the crystal period, can lead to coupling of Pauli matrices $\boldsymbol{\sigma}$ to this $\mathbf{h}(\mathbf{r})$. This would result in a magnetic mechanism of $\boldsymbol{k}$-dependent spin splitting, suggestive of a new type of spin-orbit coupling. Because the $\boldsymbol{k} \cdot \boldsymbol{p}$ formalism used in Ref. [23] did not afford an atomistic definition of $\mathbf{h}(\mathbf{r})$ and its ensuing spin splitting, nor did it provide for guiding principles to select a target material for investigating such effects, examination of these 1964 ideas remained dormant for a long time.

In the present paper, inspired by Ref. [23], we demonstrate an AFM mechanism that creates $\boldsymbol{k}$-dependent spin splitting $\Delta_{ss}(\boldsymbol{k})$ even in centrosymmetric, low-Z compounds, persists even at time-reversal invariant wave vectors, and has an unusual quadratic scaling on momentum $\boldsymbol{k}$. The coupling of spin to lattice degrees of freedom via the periodic spatial dependent intrinsic magnetic field $\mathbf{h}(\mathbf{r})$ is analogous to a new form of spin-orbit *coupling*; the fact that spin splitting can, however, exist even in absence of the electrical mechanism of the spin-orbit *interaction* in the Hamiltonian is noteworthy. We formulate the general magnetic space group conditions ("design principles") for spin splitting in different AFM prototypes, either with or without SOC, and illustrate via detailed first-principles calculations a case of purely AFM-induced spin splitting.

II. MAGNETIC SYMMETRY CONDITIONS FOR AFM-INDUCED SPIN SPLITTING

A. Symmetries that enforce spin degeneracy

To select a compound for direct magnetic $\boldsymbol{k}$-dependent spin splitting we inspect the underlying symmetry requirements. We first list the symmetries that *preserve* spin degeneracy, preventing spin splitting (SS), then discuss how to violate those symmetries. (i) As is known [24], the combination θI of time reversal θ and spatial inversion I symmetries ensures double degeneracy for arbitrary wave vector $\boldsymbol{k}$. Likewise, (ii) when SOC is turned off, the spin and spatial degrees of freedom are decoupled, so there could exist pure spin rotation U, a spinor symmetry, that reverses the spin but keeps momentum invariance, thus preserving spin degeneracy for all wave vectors. The spin rotation U does not exist in AFM when the alternating magnetic moments reside on different atomic sites, because such arrangement reverses the antiferromagnetic order. But in a specific type of AFM compound [referred to as magnetic space group (MSG) type IV [25], such as $BiCoO_3$ [20]] where there exists a translation T that

transforms the reversed antiferromagnetic order back, UT symmetry would still preserve spin degeneracy for all wave vectors.

B. Violating degeneracy-enforcing symmetries

(i) As expected, the appearance of spin splitting requires first the violation of θI symmetry. In magnetic crystals, where θ is already violated due to magnetic order, absence of the inversion I symmetry doesn't mean breaking of θI, hence it does not necessarily lead to the removal of spin degeneracy. (Actually, even for a *centrosymmetric* magnetic structure, where I is preserved but θI is broken, one can still have spin splitting.) (ii) To have SOC-unrelated spin splitting, one needs also to violate UT symmetry; here and below, when the mechanism of SOC is not specified SOC stands for the traditional electric mechanism. AFM structures that violate UT symmetry correspond to the so-called MSG type III or I such as rutile MnF_2. Appendix A provides a more detailed discussion of UT symmetries.

C. Resulting prototypes of AFM SS

Based on whether the AFM compound in question has or lacks θI symmetry, and weather it belongs to MSG type IV or MSG type I/III, we have identified four distinct types of AFM spin splitting prototypes (Table I). The first two prototypes, (1) and (2), preserve spin degeneracy at arbitrary $\boldsymbol{k}$ point because of its protection by θI symmetry. In the prototypes (3) and (4) θI is violated, allowing spin splitting in the presence of SOC. Prototype (3) being MSG type IV has spin degeneracy when SOC is turned off (referred to as "SOC-induced spin splitting") whereas prototype (4) being MSG type I or III allows spin splitting even when SOC is turned off (referred to as "AFM-induced spin splitting"). To find specific compound realizations of the four AFM prototypes (last line of Table I) we searched the listings of magnetic symmetries (such as the MAGNDATA in Bilbao listing [26]) for compliance with our symmetry conditions (top two lines in Table I). As a concrete example, we illustrate the identification of a specific realization of the AFM SS prototype 4 compound selecting by the "design principle" (symmetry condition of prototype 4): (1) MSG has no θI symmetry and (2) MSG type is I or III. We have identified a few AFM compounds as AFM SS prototype 4, e.g., MnF_2 (MSG: $P4_2'/mnm'$) [27], La_2NiO_4 (MSG: $Pc'c'n$) [28], and $ScFeO_3$ (MSG: Cc') [29]. We found that tetragonal MnF_2—with only two formula units per magnetic unit cell and with the magnetic moment on Mn aligning along the principle fourfold axis—to be a potential attractive compound for experimentalists to measure this spin-splitting physics. Tetragonal MnF_2 having magnetic space group $P4_2'/mnm'$ complies with the above noted design principles—(1) has no θI symmetry despite the presence of inversion symmetry; (2) belongs to MSG type III, therefore it has no UT symmetry.

Table I indicates that not all AFM compounds have the same SS behavior, and that the magnetic, not just spatial, symmetries are important. For example, an AFM SS has been theoretically analyzed recently based on tight-binding models on the multipole description by Hayami *et al.* [34,35]. However,

TABLE I. Classification of four spin splitting prototypes in antiferromagnetic compounds in terms of symmetry conditions, consequences, and examples. *Symmetry conditions:* θ represents time reversal and I represents spatial inversion, θI is the combination of these two operations. AFM can be MSG type I, III, or IV. (For detailed description of MSG and MSG type please refer to Appendix A.) *Consequences:* No SS means no spin splitting either with or without SOC. SOC-induced SS means that one has spin splitting when SOC is nonzero, but no spin splitting when SOC is turned off. AFM-induced SS means that one has spin splitting even when SOC is turned off. Note that the symmetry-based conditions generally apply not only to collinear but also to noncollinear AFM. For example, we would expect AFM-induced spin splitting in a noncollinear AFM Mn₃Ir [30] which is also centrosymmetric but has no θI symmetry and belongs to MSG type III.

AFM SS prototype	1	2	3	4
Condition 1: Has θI?	Yes	Yes	No	No
Condition 2: MSG type	III	IV	IV	I or III
Consequences	no SS	no SS	SOC-induced SS	AFM-induced SS
Examples	CuMnAs [31]	NiO [32]	BiCoO₃ [33]	MnF₂

their multipole analysis was based on point-group symmetry rather than the magnetic group symmetry, with nonmagnetic atoms omitted. This omission (e.g., MnF₂ without F), however, restores the UT symmetry and results in the prediction of spin degeneracy in the absence of SOC, in sharp contrast with DFT predicted (see below) giant spin splitting (see Appendix B for detailed discussion of the previous work).

III. ILLUSTRATION OF THE PROPERTIES OF AN AFM-INDUCED SS COMPOUND MnF₂

A. System

MnF₂ is a wide gap insulator both below and above its Néel temperature of 67 K [36]. It is a centrosymmetric rutile structure (conventional space group $P4_2/mnm$), with magnetic Mn ions occupying position (0, 0, 0) and (1/2, 1/2, 1/2) centered in an octahedral of nonmagnetic F anions located at $\pm(u, u, 0)$ and $\pm(1/2 + u, 1/2 − u, 1/2)$ where u is the positional parameter. The refinement x-ray-diffraction results [37] gave the positional parameter $u = 0.305$, and lattice constants $a = b = 4.873$ Å, $c = 3.311$ Å. Erickson [27] found via neutron-scattering measurements the AFM moment aligned along the tetragonal axis (i.e., [001]) with magnetic space group $P4_2'/mnm'$. The magnetic crystal unit cell is shown in Fig. 1(a). While concentrating on this specific material MnF₂ as an illustration of the physical effect, we do not maintain that it is optimized for technological usage in a specific spintronics device application (size of band gap, dopability, value of Néel temperature). Optimization of such material constants might be possible by comparing different compounds belonging to a given AFM SS prototype. This is outside the scope of the current paper.

B. Six predicted characteristics of AFM-induced spin splitting in MnF₂

We calculated the relativistic electronic structure of AFM MnF₂ within density functional theory (DFT) (see description of the DFT method in Appendix C). Figure 1(b) provides the calculated magnetization $m_z(\mathbf{r}) = m^\uparrow(\mathbf{r}) − m^\downarrow(\mathbf{r})$ in the $z = c/2$ plane, with $m^\uparrow$ and $m^\downarrow(\mathbf{r})$ representing the up- and down-spin electron density. To assess the AFM magnetism effect, we also define a reference NM model, where the magnetic moment on each site is zero, resulting in a metallic state. We emphasize that the NM model is not used to mimic the

physical high-temperature paramagnetic (PM) phase that has a distribution of nonvanishing local magnetic moments that creates an insulating gap even in the absence of long-range order [40,41]. Figure 1(c) gives the band structure of the AFM phase calculated with SOC in its experimental crystal structure. We find a z-oriented magnetic moment on Mn²⁺ of $4.7\mu_B$, in good agreement with the neutron-scattering measurement of $4.6\mu_B$. We also find a calculated minimum direct gap at Γ of 4.02 eV and a smaller indirect gap between VBM at X and CBM at Γ of 3.98 eV, comparable with the measured absorption gap [42] of 4.10 eV (estimated from the convergence limit of the observed series of discrete d-d^* multiplet transitions into the onset of band-to-band continuum). The DFT (mean-field) calculated band gap and DFT local moment both agree with experiment, providing strong evidence that the single-particle band structure picture with a 5 eV wide band width as advanced in the DFT calculations holds well, supporting the notion of well-defined coherent bands.

To assist future measurements of the predicted AFM-induced $\mathbf{k}$-dependent spin splitting [e.g., via angle-resolved photoemission spectroscopy (ARPES) and spin ARPES] as well as potential applications in novel spintronics we next describe the main predicted features of the AFM-induced spin splitting:

(i) *The spin splitting has a typical atomiclike energy scale ("giant splitting").* Despite rather small atomic numbers in MnF₂ [Z(Mn) = 25 and Z(F) = 9], the magnitude of the spin splitting [up to 300 meV seen between $V3$ and $V4$ along Γ-M in Fig. 1(e)] arising from the AFM mechanism can be comparable to some of the largest known spin splitting of conventional electric mechanism for heavy atom high-Z compounds, such as the "giant SOC"-induced spin splitting in BiTeI [43] and GeTe [44,45]. The locality of magnetic moments needed for obtaining large spin splitting does not contradict the requirement to introduce itinerant carriers. Local magnetic moments of $4−5\mu_B$ are common in Mn salts with broad (4–5 eV) bands and high electronic mobility, e.g., La$_{1−x}$Sr$_x$MnO₃ [46]. We find that the spin split bands in MnF₂ occur about 40 meV below the VBM (bands $V1$-$V2$ in Fig. 1) and about 500 meV below the VBM (bands $V3$-$V4$ in Fig. 1). Either should be amenable to photoemission detection for validating the theory. In general, for transport application requiring the creation of free carriers, one should place the Fermi level in the proximity of the split band, e.g., by doping. For MnF₂, the spin-active band $V1$ with dispersion along the
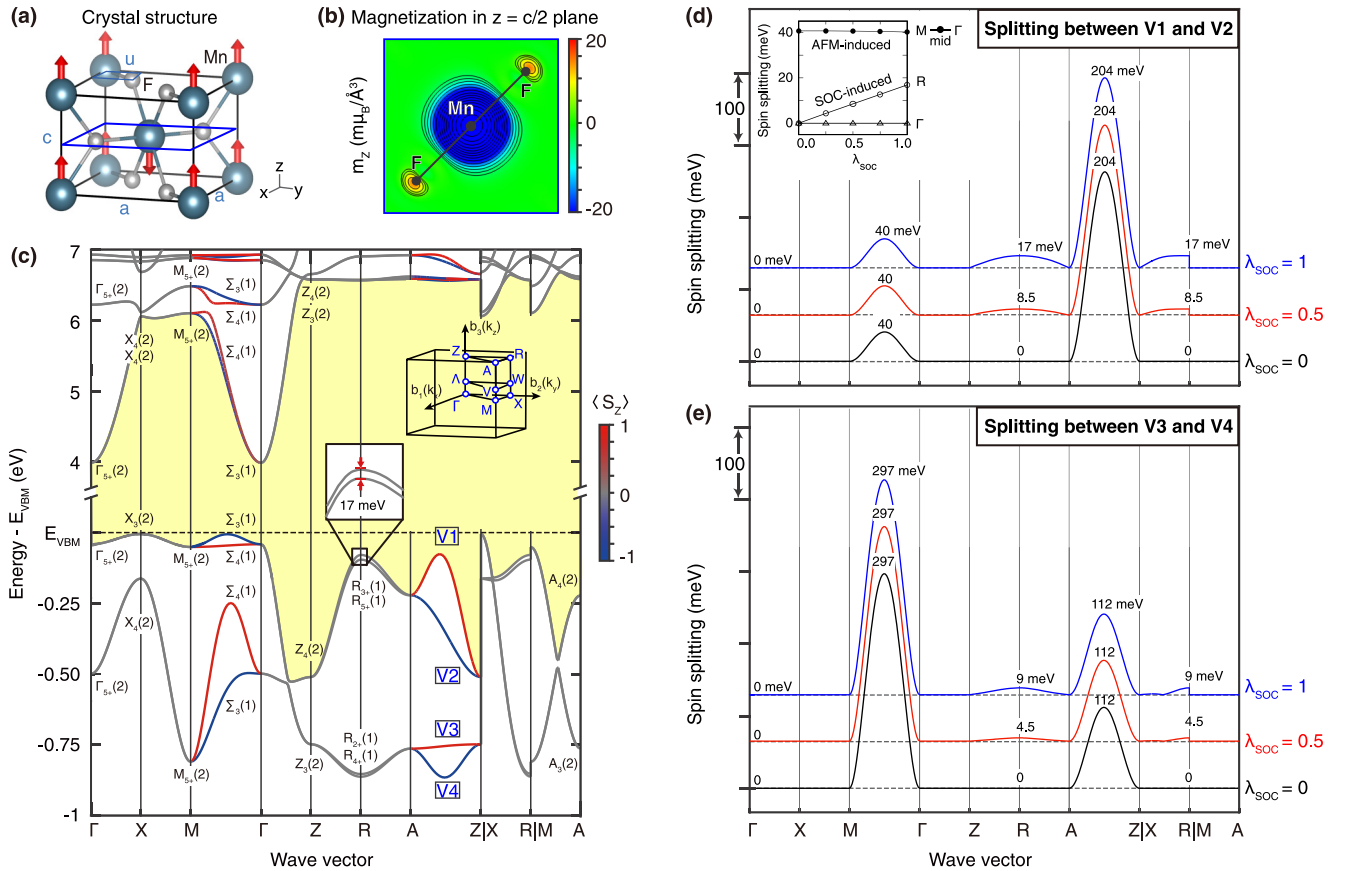
FIG. 1. Crystal structure, band structure, and spin splitting of the centrosymmetric AFM tetragonal MnF$_2$. (a) Magnetic unit cell where red arrows indicate local magnetic moment; (b) contour plot of magnetization along z in $z = c/2$ plane; (c) DFT calculated band structure with our calculated magnetic symmetry representations (see Appendix C), using the notations of Ref. [38] with numbers in parentheses indicating the dimension of the representation (i.e., degeneracies). The top four valence bands are denoted by $V1$, $V2$, $V3$, $V4$ and the yellow screen highlights the gaps between valence and conduction bands. Inset of (c) shows the BZ and the blow-up bands around R point. The blue to red color scale denotes the calculated out-of-plane spin polarization. Panels (d) and (e) show DFT calculated wave-vector dependence of the spin splitting between pairs of valence bands $V1$ and $V2$ [in (d)] and between $V3$ and $V4$ [in (e)] for different scaling of SOC λ_{SOC} (numerical coefficient $0 < \lambda_{SOC} < 1$). Inset of (d) shows the spin splitting vs the amplitude of the spin-orbit coupling λ_{SOC} at Γ (0, 0, 0), R (0, 0.5, 0.5), and the middle point of Γ-M (0.25, 0.25, 0). All DFT calculations use PBE exchange correlation functional [39] with on-site Coulomb interaction on Mn-3d orbitals of $U = 5$ eV, $J = 0$ eV, and the experimental crystal structure [37].

M-Γ direction is just 1 meV below VBM at X [see Fig. 1(c)], so in this case it does not pose a problem. The $V3$-$V4$ bands in MnF$_2$ are not optimal for creation of free carriers as they are rather deep.

(ii) *The splitting persists even if SOC = 0.* The spin splitting along the Γ-M and Z-A lines is present even when SOC is turned off in the Hamiltonian [black line in Figs. 1(d) and 1(e), also shown in the inset of (d)]. This is very different from prototype 3 AFM (Table I) BiCoO$_3$ [20], where spin splitting disappears if SOC vanishes. Thus, the AFM-induced spin splitting mechanism delivers the long-standing hope for a wave-vector-dependent spin splitting mechanism in thermo-dynamically stable, low-Z compounds.

(iii) *Relative to the NM case, AFM induces a highly anisotropic and **k**-dependent spin splitting.* We show in Fig. 2 the band structures of centrosymmetric MnF$_2$ in two cases: (a) NM without SOC; (b) AFM without SOC. In both cases we indicate the degeneracies of states, calculated by DFT shown as integer values. An important manifestation of the AFM-induced spin splitting [Fig. 1(c)] is that whereas in the

NM structure, the whole BZ, including directions Γ-X and Γ-M, have doubly degenerate (nonsplit) bands, in the AFM structure spin splitting arises even in the absence of SOC but it is wave-vector dependent. Bands remain degenerate along the Γ-X directions, but become spin split along the Γ-M direction. Such anisotropic spin splitting was already hinted by the asymmetry in magnetization in coordinate space as shown in Fig. 1(b) between $\boldsymbol{x} + \boldsymbol{y}$, $\boldsymbol{x} - \boldsymbol{y}$, and $\boldsymbol{x}$, $\boldsymbol{y}$ directions. This behavior is understandable on the basis of magnetic symmetry (see Appendix A for a discussion of unitary and antiunitary symmetries): the AFM ordering does not lead to symmetry reduction along the Γ-X paths, relative to its NM counterpart. The resulting spin degeneracy along the k_x (or k_y) direction of Γ-X in AFM is protected by its group of **k** symmetries $\theta\{C_{2x}|\boldsymbol{\tau}\}$ and $\theta\{\sigma_{vy}|\boldsymbol{\tau}\}$ (or $\theta\{C_{2y}|\boldsymbol{\tau}\}$ and $\theta\{\sigma_{vx}|\boldsymbol{\tau}\}$). In contrast, along the Γ-M paths, in AFM the combined symmetries of $\theta\{C_{2a}|0\}$ and $\theta\{C_{2b}|0\}$ (or $\theta\{\sigma_{da}|0\}$ and $\theta\{\sigma_{db}|0\}$) are broken, which creates spin splitting. Here, C_{2x}, C_{2y}, C_{2a}, C_{2b} are π rotations about the [100], [010], [110], [1$\bar{1}$0] axes, respectively; σ_{vx}, σ_{vy}, σ_{da}, σ_{db} are mirror reflections in (100), (010),
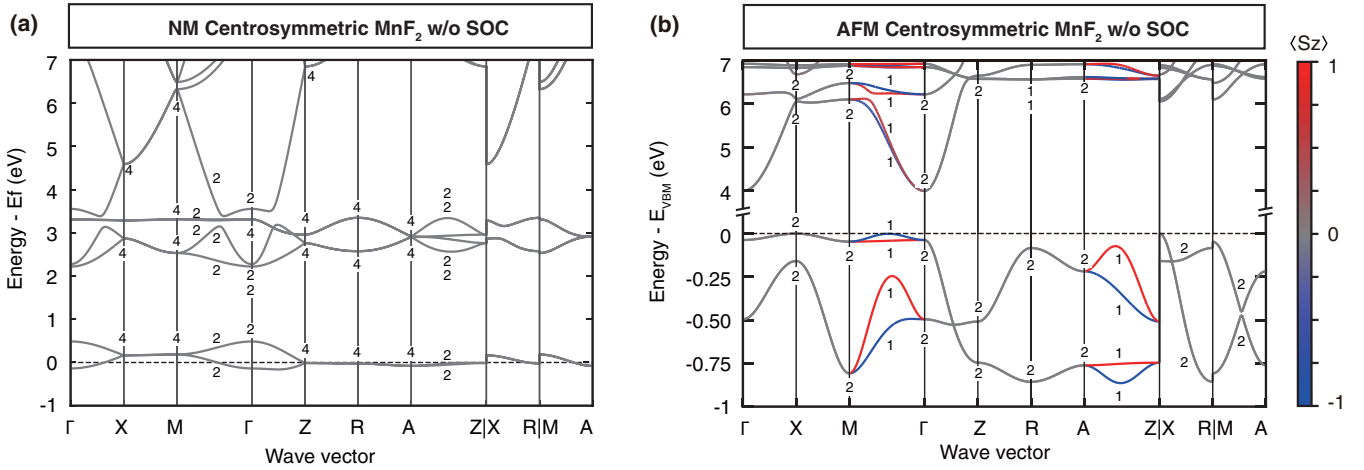
FIG. 2. DFT band structures of centrosymmetric (CS) MnF_2 in NM and AFM without SOC. In all cases we use the experimentally observed centrosymmetric tetragonal structure [37]: (a) NM with SOC set to zero; (b) AFM with SOC set to zero. Out-of-plane spin polarizations are mapped to color scale from blue to red. The integer number attached to each band and k point is the degeneracies.

(1-10), (110) planes; and vector $\tau = (1/2, 1/2, 1/2)$ is half lattice translation, directed along the spatial diagonal [111] of the unit cell. Similar arguments (given in Appendix D) apply for spin degeneracy along Z-R and spin splitting along Z-A in Fig. 1(b).

(iv) *The AFM mechanism gives rise to even powers of k in the spin splitting.* Of special interest in Fig. 1(c) is the diagonal Γ-M and the Z-A lines showing large spin splitting while at the end of these k lines the splitting vanishes. It is of interest therefore, to establish how the splitting changes near its k-space end points. By fitting the DFT calculated spin splitting $\Delta_{ss}(k)$ to the power of k, we found a quadratic-in-k dependence at $\Gamma_{\Gamma-M}$ (i.e., near the Γ end along the $\Gamma-M$ path) and $M_{M-\Gamma}$ (see details of fitting in Appendix E and effective model in Appendix F). Thus, near the degeneracy points $\Delta_{ss}(k)$ shows a quadratic k dependence compared with the odd powers typical of the electrically induced SOC effect.

(v) *A Dresselhaus in-plane spin texture results from the cooperative SOC and AFM effects.* The coupling between spin space and positional space results not only in the spin splitting of the energy spectrum, but also in developing "spin-momentum locking," where the spin orientation is locked with momentum k. The vector field of the spin states in momentum space is called spin texture, being helical for the conventional Rashba SOC mechanism [2] and nonhelical for the Dresselhaus mechanism [1]. The spin texture for AFM-induced spin splitting has its own fingerprints. Figure 3 shows the calculated spin textures of the $V1$ and $V2$ bands at the representative k plane $k_z = \pi/2c$ where c is the lattice constant along the z axis. We see that electron spins are mostly aligned along the out-of-plane z direction, as can be surmized from the magnetic structure [see Fig. 1(a)]. This is seen in the four quadrants patterns on a fixed k_z plane with positive [up arrow in Figs. 3(a) and 3(b)] and negative [down arrow in Figs. 3(a) and 3(b)] out-of-plane spin polarizations in the neighbor quadrants. The out-of-plane spin polarizations are opposite in sign between bands $V1$ and $V2$, as noted by the reversal of the red and blue patterns for $V1$ and $V2$. A similar four-quadrant pattern of out-of-plane spin polarization

is also found in the $k_z = 0$ and $k_z = \pi/c$ planes (see the corresponding spin texture results in Appendix G).

Interestingly, inspecting the $k_z = \pi/2c$ plane, Fig. 3 shows a pronounced (i) in-plane and (ii) nonhelical Dresselhaus-like spin texture. These features are unexpected given that the crystal structure of MnF_2 is magnetized in the z direction and is centrosymmetric, while normally to assure Dresselhaus features [3] noncentrosymmetric symmetry is needed. We find that the Dresselhaus spin texture in MnF_2 requires for its existence the SOC term (i.e., the texture vanishes if the SOC is removed from the Hamiltonian). Thus, the texture represents the combined effect of coexistence of SOC with AFM (see cooperative effect on spin splitting in Appendix H).

(vi) *Spin splitting at different wave vectors can have different dependence on SOC strength:* The insert of Fig. 1(d) shows different characteristic behaviors of the dependence of spin splitting $\Delta_{ss}(k)$ on spin-orbit strength at different k points: (1) The trivial case (e.g., Γ point) is that neither magnetic
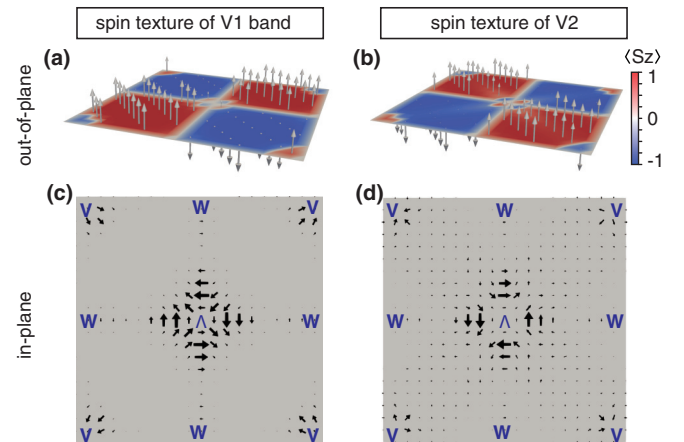
FIG. 3. Spin textures in AFM MnF_2 with SOC on $k_z = \pi/2c$ plane. (a) Out-of-plane spin texture of $V1$ band, (b) out-of-plane spin texture of $V2$ band, (c) in-plane spin texture of $V1$ band, and (d) in-plane spin texture of $V2$ band.

nor electric SOC induces any splitting; (2) the R point shows zero spin splitting when $\lambda_{SOC} = 0$ and linear dependence of λ_{SOC}, illustrating a cooperation of both magnetic and SOC mechanisms; notice that despite R being a TRIM point, it shows spin splitting, unlike the case of purely SOC-induced effects; (3) the nontrivial case of purely magnetic-induced spin splitting occurs along the Γ-M (as well as A-Z) line, where nonzero spin splitting is present even at $\lambda_{SOC} = 0$ and is almost independent of λ_{SOC}. The appearance of such distinct spin splitting behaviors at different wave vectors in a single compound would be advocated for multifunctional spintronic applications.

IV. DISCUSSION

This study uncovers the design principles of spin splitting in AFM compounds based on magnetic symmetry analysis and shows a very rich set of fingerprint fundamental physical effects [(i)–(vi) above] in a specific prototype, including the giant spin splitting that characterizes the AFM mechanism and could aid its future experimental observation.

While the present paper focuses on the fundamental physics of a prototype case of antiferromagnetically induced k-dependent spin splitting even without the presence of SOC or absence of spatial inversion, we might discuss general anticipated connections with experiment and applications. Nevertheless, a number of recent experimental papers may have future connections to the current theory. As an example, active research is currently taking place on two-dimensional (2D) layered systems consisting of two layers, of which one is an AFM and the other a heavy metal such as Pt, with the SOC of Rashba type developing on their interface and controlled by electric bias applied across it [47,48]. Using instead antiferromagnets with spin-split bands described in the current paper, which in addition are either magnetoelectric or piezoelectric, might eliminate the need for a heavy-metal layer, as the current AFM magnetic mechanism provides a giant magnitude of spin-orbit splitting even with light elements. Similarly, the observation by Tazaki *et al.* [49] of large current-induced magnetic torque *in a low-Z magnet* suggests the possibility worth perhaps examining of the presence of the magnetic mechanism such as described in the current paper as an alternative to the conventional SOC mechanism. Recently, Geprägs *et al.* [50] showed that spin Hall magnetoresistance allows obtaining valuable information on the spin texture via straightforward electrical transport measurements, a technique that could be applicable to detect our predicted AFM-induced spin texture (Fig. 3). Högl *et al.* [51] studied graphene on antiferromagnet substrate expecting a strong quantum anomalous Hall effect from the antiferromagnet substrate, raising the possibility that the currently explored 3D AFM systems could be suitable interesting substrates. We also note a few transport effects that are likely associated with the AFM-induced spin splitting effect. These include finite spin current predicted by Železný *et al.* [52], anomalous Hall conductivity predicted by Chen *et al.* [53] and Suzuki *et al.* [54], and crystal Hall effect proposed [55] by Šmejkal *et al.* and verified [56] by Feng *et al.*

APPENDIX A: ADDITIONAL SYMMETRY CONSIDERATIONS BEYOND θI FOR SELECTING COMPOUNDS HAVING NONZERO MAGNETIC-INDUCED SPIN SPLITTING

To select magnetic crystals that have nonzero contribution from the magnetic mechanism means to find the crystals that still have k-dependent spin splitting even in the absence of SOC (i.e., when there is no contribution from the electric mechanism). To do so one must violate UT symmetry, where U is a spinor symmetry of SU(2) which reverses the spin state and T is a translation of the primitive lattice. This requirement stems from the fact that the existence of UT symmetry preserves the double degeneracy in the whole Brillouin zone, as it transfers any spin state to its opposite spin state while keeping k invariant for arbitrary wave vector. Such UT symmetry exists in AFM compounds whose magnetic unit cell is not equivalent to its nonmagnetic unit cell: the primitive lattice translation T translates those up-spin (down-spin) atoms to occupy the down-spin (up-spin) atom sites while U reverses the spin, thus UT symmetry preserves the crystal structure.

Antiferromagnets with primitive lattice translations that reverse the microscopic magnetic moments are formally known as having black and white Bravais lattice and type-IV in terms of magnetic space group (MSG). Formally, the MSG includes not only the unitary symmetries (USs), i.e., spatial symmetries, but also antiunitary symmetries (ASs), that are time reversal θ and its combination with spatial operations.

In terms of its construction of the unitary and antiunitary part from the space group (G), MSG can be classified into four types:

(i) MSG that has no antiunitary symmetries (i.e., AS $= \emptyset$) are identified as MSG type I.

(ii) MSG that has the unitary part equivalent to G and an equal number of antiunitary symmetries, *i.e.,* US $= G$, AS $= \theta G$ belongs to MSG type II. Since all NM cases have time-reversal symmetry, they all belong to this category.

(iii) MSG that has the unitary part composed of half of its magnetic space-group symmetries (spatial operations that keep the atomic structure invariant) is MSG type III or type IV: if the system has a normal Bravais lattice (magnetic unit cell equivalent to its NM primitive unit cell) it is MSG type III; if the system has a black and white Bravais lattice (magnetic

unit cell being supercell of its NM primitive unit cell) it is MSG type IV.

AFM with antiferromagnetic order spontaneously breaks time-reversal symmetry and therefore can't be MSG type II but can be MSG type I, III, or IV.

Our selected AFM compound MnF_2 has magnetic space group $P4_2'/mn'm$ without SOC and the space group $P4_2'/mnm'$ with SOC, both of which belong to MSG type III with equivalent AFM unit cell (Mn_2F_4) to the NM primitive unit cell (Mn_2F_4). Therefore, it is expected to have spin splitting in such an AFM compound from symmetry perspective.

APPENDIX B: PREVIOUS STUDIES ON SPIN SPLITTING IN AFM COMPOUNDS

There are many previous works on spin splitting in AFM compounds. While most of the studies mentioned the occurrence of spin splitting, only a few literatures tried to establish a causal understanding of such a phenomenon. To give a clear view of the conceptional advance of this paper, here we list several previous studies on the spin splitting in AFM and compare them to this work.

1. Previous studies on the occurrence of spin splitting in AFM compounds

Hu *et al.* [17] predicted that iron-pnictide AFM $BaCrFeAs_2$ could be half metallic due to the spin splitting, by first-principles and tight-binding calculations. Gao *et al.* [18] predicted AFM Mn_3Al and Mn_3Ga to have spin splitting by first-principles calculation. Gong *et al.* [19] showed that 2D van der Waals AFM materials could have spin splitting under density functional theory. In this work, we are not satisfied with only showing the existence of spin splitting in AFM without the need of SOC (to aid experimental testing); more importantly, we formulate the fundamental magnetic space-group conditions ("design principles") for spin splitting in the absence of SOC—violation of both θI and UT symmetries.

2. Previous studies on the causal understanding of spin splitting in AFM

As far as we know, the first literature of the causal understanding was from one of our co-workers, Emmanuel Rashba [23], which has already been discussed in the main text. Other previous works include Hayami *et al.* [34], who examined AFM spin splitting when SOC is absent, by using tight-binding model on the multipole description based on point-group symmetry of the magnetic element. In this work we have found that the complete symmetry analysis should also include nonmagnetic atoms and the translational symmetry, meaning the magnetic group symmetry. For example, in the case of tetragonal MnF_2, removing the nonmagnetic F^- anions will restore the UT symmetry and result in a complete spin degeneracy in the absence of SOC, in sharp contrast to our DFT predicted giant spin splitting. To address the real-life case where SOC is finite, in this work we also have discussed both cases when SOC is present and absent.

Another previous work, by Naka *et al.* [35], shows in a specific type of organic antiferromagnet the spin splitting effect can be used for spin current generation. The authors

described the spin splitting effect as originating from unspecified AFM order induced by real-space molecular arrangement anisotropy in a class of organic antiferromagnets. However, the descriptive understanding is specific to organic antiferromagnet with checker-plate-type lattice. While in this work we have offered more general design principles, not specialized for any specific systems, the design principles are based on the magnetic symmetry and hence are easy to apply to predictions of a real compound with the properties discussed.

APPENDIX C: DFT CALCULATION METHODS AND PARAMETERS

1. DFT calculation parameters

We have studied the electronic and spin properties of MnF_2 using DFT with the experimental crystal structure [37] and the experimental spin configuration [27]. In the DFT calculations, we use Perdew-Burke-Ernzerhof (PBE) exchange correlation functional [39] with plane-wave basis (energy cutoff of 500 eV and $10 \times 10 \times 14$ Monkhorst-pack k-mesh sampling [57]). We use the on-site potentials of $U = 5\,\text{eV}$ and $J = 0\,\text{eV}$ on Mn $3d$ orbitals following the Liechtenstein approach [58].

2. Controlling SOC strength in AFM and NM

Band structures under different (artificial) SO strengths are calculated by introducing a numerical prefactor λ_{SOC} $(0 < \lambda_{\text{SOC}} < 1)$ to the SO Hamiltonian term $\lambda_{\text{SOC}}(\frac{\hbar}{2m_e^2c^2}\frac{K(r)}{r}\frac{dV(r)}{dr}\hat{L} \cdot \hat{S})$ in the DFT formalism [59], where $\hat{L} = \hat{r} \times \hat{p}$ is the orbital angular momentum operator, $\hat{S}$ is the spin operator, $V(r)$ is the spherical part of the effective all-electron potential within the projector augmented plane-wave (PAW) sphere, and $K(r) = (1 - \frac{V(r)}{2m_ec^2})^{-2}$. Hamiltonians (as well as wave functions, charge density, and $V(r)$, etc.) are still calculated self-consistently. To study the effect of magnetic mechanism we use a reference NM model where the magnetic moment on each atomic site is zero. We emphasize that the NM model is not used to mimic the physical high-temperature paramagnetic phase that has zero total moment but a distribution of nonvanishing local magnetic moments that creates an insulating gap even in the absence of long-range order [40,41].

3. Spin polarization and spin texture calculations

The spin polarization for Bloch state $|\mathbf{k}\rangle$ is calculated via the definition of $\langle \mathbf{k}|\hat{S}|\mathbf{k}\rangle$, which can be decomposed into two components: the out-of-plane spin polarization $\langle \mathbf{k}|\hat{S}_z|\mathbf{k}\rangle$ and the in-plane spin polarization $\langle \mathbf{k}|(\hat{S}_x, \hat{S}_y)|\mathbf{k}\rangle$. The spin texture of selected bands on the $\mathbf{k}$ plane is calculated by evaluating both the out-of-plane and in-plane spin polarizations for each $|\mathbf{k}\rangle$ on the $\mathbf{k}$ plane.

4. Representations for bands

The double group irreducible (*co*) representation for each degenerate state at the high-symmetry $\mathbf{k}$ point of the AFM phase with SOC is derived by the following: (a) We first calculate the transformation properties of selected Bloch basis states under the relevant group of $\mathbf{k}$ symmetries; the Bloch basis is constructed to have the same spin and orbital character

TABLE II. Unitary and antiunitary symmetries of MnF$_2$ with inclusion and exclusion of SOC in NM and AFM phases.

MnF$_2$	w/o SOC	w/ SOC
NM	Space group: $P4_2/mnm$	Double space group: $P4_2/mnm$
	G_U : $H, LH1, LH2, LH3$	G_U : $H, LH1, LH2, LH3, H_D, LH1_D, LH2_D, LH3_D$
	G_{AU} : $H', LH1', LH2', LH3'$	G_{AU} : $H', LH1', LH2', LH3', H'_D, LH1'_D, LH2'_D, LH3'_D$
AFM	Magnetic space group: $P4_2'/mn'm$	Magnetic double space group: $P4_2'/mnm'$
	G_U : $H, LH1$	G_U : $H, LH2, H_D, LH2_D$
	G_{AU} : $LH2', LH3'$	G_{AU} : $LH1', LH3', LH1'_D, LH3'_D$

(obtained from DFT) and the ensuring transformation properties of the degenerate states. (b) We then identify and label the degenerate bands at such k points adopting the names of irreducible (co) representations for MnF$_2$ from Ref. [38]. (c) Whether additional degeneracy will be induced by antiunitary symmetries is determined using Wigner's test [25] given in Ref. [38].

APPENDIX D: SYMMETRY ANALYSIS OF BAND EIGENSTATES IN MnF$_2$

The spin degeneracy and splitting are direct consequences of symmetry preservations and reductions upon introducing AFM and SOC. We see that it is the introducing of antiferromagnetic order from the NM to AFM phase of MnF$_2$ that breaks the fourfold axial symmetry and makes directions $\langle 100 \rangle$ and $\langle 110 \rangle$ nonequivalent. Such symmetry breaking manifests itself dramatically in the anisotropic spin splitting of electron bands; see Fig. 1(c).

1. Symmetry protected spin degeneracy

Given the Hamiltonian $\hat{H}$ and one of its eigenvectors ψ with eigenvalue E, for any symmetry $\hat{g}$ of $\hat{H}$ (that has $[\hat{g}, \hat{H}] = 0$), $\hat{g}\psi$ is also an eigenvector of $\hat{H}$ with the same eigenvalue E. This is easily verified as

$$\hat{H}\hat{g}\psi = \hat{g}\hat{H}\psi = E\hat{g}\psi. \tag{D1}$$

When ψ and $\hat{g}\psi$ are linear independent states, they form a pair of degenerate states; the spin degeneracy at specific k points can then be protected if $\hat{g}$ also keeps k invariant, i.e., $\hat{g}k = k + G$ (where G is the reciprocal-lattice vector). For example, for

$\hat{g}$ being the TR symmetry and $[\hat{g}, \hat{H}] = 0$, $\hat{g}$ enforces doubly spin degeneracy at TRIM points.

2. Space groups and symmetry operators for MnF$_2$ NM and AFM phases, with and without SOC

If one does not consider the time-reversal symmetry θ, the space group G of NM MnF$_2$ is $P4_2/mnm$, consisting of 16 unitary symmetries. Using the subgroup $H = \{E, C_2, I, \sigma_h\}$ of G (index $[G : H] = 4$), we can write the partition of G using H and its three left cosets $LH1$, $LH2$, and $LH3$ as listed in Table II. See Table III for the explicit list of symmetry operations of H, LH1, LH2, and LH3.

Here E is the identity; I is the spatial inversion; C_2, C_{2x}, C_{2y}, C_{2a}, C_{2b} are π rotations about the [001], [100], [010], [110], [1–10] axes, respectively; σ_h, σ_{vx}, σ_{vy}, σ_{da}, σ_{db} are reflections in (001), (100), (010), (1-10), (110) planes, respectively; C_4 and C_4^- are counterclockwise and clockwise $\pi/2$ rotations about the (001) axis; S_4 and S_4^- are counterclockwise and clockwise $\pi/2$ rotations about the (001) axis followed by an inversion; vector $\boldsymbol{\tau} = (1/2, 1/2, 1/2)$ is half lattice translation, directed along the spatial diagonal [111] of the unit cell.

When considering the time-reversal symmetry θ, the 16 unitary symmetries form a subgroup $G_U = H + LH1 + LH2 + LH3$, while the NM system also has θ combined with all 16 unitary symmetries in G_U, leading to an antiunitary set G_{AU}. Using the prime symbol to indicate time-reversal symmetry, we have $G_{AU} = G'_U = \theta G_U$. The entire group now becomes $G = G_U + G_{AU} = G_U + G'_U = H + LH1 + LH2 + LH3 + H' + LH1' + LH2' + LH3'$.

Including SOC in NM couples the spatial rotation to spin rotation, which results in a double space group of $P4_2/mnm$

TABLE III. Explicit lists of space-group symmetries of NM MnF$_2$.

H	$LH1 = \{C_{2a}|0\}H$
$\{E\|0\}$: $(x, y, z) \rightarrow (x, y, z)$	$\{C_{2a}\|0\}$: $(x, y, z) \rightarrow (y, x, -z)$
$\{C_2\|0\}$: $(x, y, z) \rightarrow (-x, -y, z)$	$\{C_{2b}\|0\}$: $(x, y, z) \rightarrow (-y, -x, -z)$
$\{I\|0\}$: $(x, y, z) \rightarrow (-x, -y, -z)$	$\{\sigma_{da}\|0\}$: $(x, y, z) \rightarrow (y, x, z)$
$\{\sigma_h\|0\}$: $(x, y, z) \rightarrow (x, y, -z)$	$\{\sigma_{db}\|0\}$: $(x, y, z) \rightarrow (-y, -x, z)$

$LH2 = \{C_{2x}|\boldsymbol{\tau}\}H$	$LH3 = \{C_4|\boldsymbol{\tau}\}H$
$\{C_{2x}\|\boldsymbol{\tau}\}$: $(x, y, z) \rightarrow (x + \frac{1}{2}, -y + \frac{1}{2}, -z + \frac{1}{2})$	$\{C_4\|\boldsymbol{\tau}\}$: $(x, y, z) \rightarrow (-y + \frac{1}{2}, x + \frac{1}{2}, z + \frac{1}{2})$
$\{C_{2y}\|\boldsymbol{\tau}\}$: $(x, y, z) \rightarrow (-x + \frac{1}{2}, y + \frac{1}{2}, -z + \frac{1}{2})$	$\{C_4^-\|\boldsymbol{\tau}\}$: $(x, y, z) \rightarrow (y + \frac{1}{2}, -x + \frac{1}{2}, z + \frac{1}{2})$
$\{\sigma_{vx}\|\boldsymbol{\tau}\}$: $(x, y, z) \rightarrow (-x + \frac{1}{2}, y + \frac{1}{2}, z + \frac{1}{2})$	$\{S_4\|\boldsymbol{\tau}\}$: $(x, y, z) \rightarrow (y + \frac{1}{2}, -x + \frac{1}{2}, -z + \frac{1}{2})$
$\{\sigma_{vy}\|\boldsymbol{\tau}\}$: $(x, y, z) \rightarrow (x + \frac{1}{2}, -y + \frac{1}{2}, z + \frac{1}{2})$	$\{S_4^-\|\boldsymbol{\tau}\}$: $(x, y, z) \rightarrow (-y + \frac{1}{2}, x + \frac{1}{2}, -z + \frac{1}{2})$

composed of H, $LH1, LH2, LH3, H', LH1', LH2', LH3'$ and their combination with a rotation of 2π ($\bar{E}$): $H_D = \{\bar{E}, \overline{C_2}, \bar{I}, \overline{\sigma_h}\}$, $LH1_D = \{C_{2a}|0\}H_D$, $LH2_D = \{C_{2x}|\tau\}H_D$, $LH3_D = \{C_4|\tau\}H_D$, and H'_D, $LH1'_D$, $LH2'_D$, $LH3'_D$. In centrosymmetric MnF$_2$, due to the presence of θI symmetry ($\theta I \in H'_D$), all bands are spin degenerates within the whole BZ.

Going from NM to AFM, the above $P4_2/mnm$ space group reduces to a magnetic group M consisting of unitary G_U and antiunitary G_{AU} parts $M = G_U + G_{AU}$. In the absence of SOC in AFM, the unitary part $G_U = H + LH1$, while the antiunitary part is $G_{AU} = LH2' + LH3'$. Including SOC in AFM couples the spatial rotation to spin rotation in the manner of one to two mapping from SO(3) to SU(2); thus, the rotations of $LH1$ and $LH2$ not only rotate the spatial space but also reverse the spin orientation. Consequently, the unitary part of the magnetic space group becomes $G_U = H + LH2 + H_D + LH2_D$, and the antiunitary part becomes $G_{AU} = LH1' + LH3' + LH1'_D + LH3'_D$. The above symmetry analysis of MnF$_2$ is summarized in Table II.

3. Different spin splitting behaviors along Γ-*X*, Γ-*M*, and *Z*-*R* directions in AFM MnF$_2$

Along the spin degenerate k path Γ-*X*, the coordinate of k is $(u, 0, 0)$ with u an arbitrary real value between 0 and 1/2. The possible symmetries that keep k invariant are [notice that all conclusions below also are applicable for $k = (0, u, 0)$ by interchanging x with y]

$$\begin{aligned}
\{E|0\} &: (u, 0, 0) \to (u, 0, 0), \\
\{\sigma_h|0\} &: (u, 0, 0) \to (u, 0, 0), \\
\{C_{2x}|\tau\} &: (u, 0, 0) \to (u, 0, 0) \quad, \\
\{\sigma_{vy}|\tau\} &: (u, 0, 0) \to (u, 0, 0), \\
\theta\{C_{2y}|\tau\} &: (u, 0, 0) \to (u, 0, 0), \\
\theta\{\sigma_{vx}|\tau\} &: (u, 0, 0) \to (u, 0, 0).
\end{aligned} \quad \text{(D2)}$$

(1) When SOC is ignored, the magnetic space group is $P4_2'/mn'm$, among above six symmetries only $\{E|0\}$, $\{\sigma_h|0\}$, $\theta\{C_{2y}|\tau\}$, and $\theta\{\sigma_{vx}|\tau\}$ are symmetries of the magnetic system, where both $\theta\{C_{2y}|\tau\}$ and $\theta\{\sigma_{vx}|\tau\}$ will transfer spin state to opposite spin state and enforce degeneracy between them.

(2) When SOC is considered, the magnetic space group is $P4_2'/mnm'$, among above six symmetries only unitary symmetries $\{E|0\}$, $\{\sigma_h|0\}$, $\{C_{2x}|\tau\}$, and $\{\sigma_{vy}|\tau\}$ are symmetries of the magnetic system, where either $\{C_{2x}|\tau\}$ or $\{\sigma_{vy}|\tau\}$ will transfer the spin eigenstate to a linearly independent spin state, therefore enforcing spin degeneracy between them. The same conclusion can also be obtained from the fact that the group of the wave vector formed by the four unitary symmetries has only one 2D double group irreducible representation Δ_5 (see Table III in Ref. [38]).

Along the spin splitting k path Γ-*M*, the coordinate of k is $(u, u, 0)$. The possible symmetries that keep k invariant are [notice that all conclusions below also are applicable for $k = (-u, u, 0)$ by interchanging a with b]

$$\begin{aligned}
\{E|0\} &: (u, u, 0) \to (u, u, 0), \\
\{\sigma_h|0\} &: (u, u, 0) \to (u, u, 0), \\
\{C_{2a}|0\} &: (u, u, 0) \to (u, u, 0) \quad, \\
\{\sigma_{db}|0\} &: (u, u, 0) \to (u, u, 0), \\
\theta\{C_{2b}|0\} &: (u, u, 0) \to (u, u, 0), \\
\theta\{\sigma_{da}|0\} &: (u, u, 0) \to (u, u, 0).
\end{aligned} \quad \text{(D3)}$$

(1) When SOC is ignored, the group of the wave vector only has four unitary symmetries $\{E|0\}$, $\{\sigma_h|0\}$, $\{C_{2a}|0\}$, and $\{\sigma_{db}|0\}$; none of these would reverse the spin state and therefore spin splitting is expected along this direction.

(2) When SOC is considered, the group of the wave vector has two unitary symmetries $\{E|0\}$, $\{\sigma_h|0\}$, and two antiunitary symmetries $\theta\{C_{2b}|0\}$, $\theta\{\sigma_{da}|0\}$. Again, none of these symmetries would reverse the spin up (down) state to its opposite, therefore spin splitting is expected in this case.

The situation becomes a bit more complicated for the k path on the boundary of BZ. Along *Z*-*R* with $k = (u, 0, 1/2)$, the possible symmetries that keep k invariant are

$$\begin{aligned}
\{E|0\} &: (u, 0, 1/2) \to (u, 0, 1/2), \\
\{\sigma_h|0\} &: (u, 0, 1/2) \to (u, 0, 1/2) - (0, 0, 1), \\
\{C_{2x}|\tau\} &: \left(u, 0, \tfrac{1}{2}\right) \to \left(u, 0, \tfrac{1}{2}\right) - (0, 0, 1) \quad, \\
\{\sigma_{vy}|\tau\} &: (u, 0, 1/2) \to (u, 0, 1/2), \\
\theta\{C_{2y}|\tau\} &: (u, 0, 1/2) \to (u, 0, 1/2), \\
\theta\{\sigma_{vx}|\tau\} &: (u, 0, 1/2) \to (u, 0, 1/2) - (0, 0, 1),
\end{aligned} \quad \text{(D4)}$$

and their combination with a primitive translation along the z axis of $\{E|(0, 0, 1)\}$.

(1) When SOC is ignored, the group of the wave vector is composed of $\{E|0\}$, $\{\sigma_h|0\}$, $\theta\{C_{2y}|\tau\}$, and $\theta\{\sigma_{vx}|\tau\}$ symmetries and their combination with $\{E|(0, 0, 1)\}$, where either $\theta\{C_{2y}|\tau\}$ or $\theta\{\sigma_{vx}|\tau\}$ will protect a double degeneracy.

(2) When SOC is considered, the group of the wave vector has only unitary symmetries $\{E|0\}$, $\{\sigma_h|0\}$, $\{C_{2x}|\tau\}$, and

TABLE IV. Power of k dependence of spin splitting in AFM MnF$_2$ with SOC. The spin splitting near given high-symmetry k_0 point and $(k_0 + \Delta k)$ are fitted to $\alpha_{k_0}|k|^\eta$ for the top two valence bands, $V1$ and $V2$, and the third and fourth valence bands, $V3$ and $V4$. Row captions like $\Gamma_{\Gamma-M}$ are used to note spin splitting near Γ along Γ-*M*.

k point	$\Delta_{\text{SS}}^{V1-V2}(k)$	$\Delta_{\text{SS}}^{V3-V4}(k)$	Linear or quadratic?
$\Gamma_{\Gamma-M}$	$0.45k^{1.98}$	$3.72k^{1.95}$	quadratic
$M_{M-\Gamma}$	$0.44k^{1.98}$	$3.86k^{1.95}$	quadratic
Z_{Z-R}	$0.04k^{0.98}$	$0.02k^{1.01}$	linear
A_{A-R}	$0.01k^{1.04}$	$0.05k^{0.98}$	linear

TABLE V. The transformation properties of symmetrized matrix and irreducible tensor up to the second order in k under symmetry operations of the group of wave vector at Γ (without SOC).

Symmetrized matrix	Irreducible tensor	$\{C_{2a}|0\}$	$\{C_{2b}|0\}$	$\{I|0\}$	$\theta\{C_{2x}|\tau\}$
σ_0	$C, k_x^2 + k_y^2, k_z^2$	1	1	1	1
σ_z	$k_x k_y$	1	1	1	-1

TABLE VI. The transformation properties of symmetrized matrix and irreducible tensor up to the second order in k under symmetry operations of the little point group at Γ (with SOC).

Symmetrized matrix	Irreducible tensor	$\{C_{2x}\vert\boldsymbol{\tau}\}$	$\{C_{2y}\vert\boldsymbol{\tau}\}$	$\{I\vert 0\}$	$\theta\{C_{2a}\vert 0\}$
σ_0	$C, k_x^2 + k_y^2, k_z^2$	1	1	1	1
σ_z	$k_x k_y$	-1	-1	1	1
(σ_x, σ_y)	$-$	$\begin{bmatrix} 1 & 0 \\ 0 & -1 \end{bmatrix}$	$\begin{bmatrix} -1 & 0 \\ 0 & 1 \end{bmatrix}$	$\begin{bmatrix} 1 & 0 \\ 0 & 1 \end{bmatrix}$	$\begin{bmatrix} 0 & -1 \\ -1 & 0 \end{bmatrix}$

$\{\sigma_{vy}\vert\boldsymbol{\tau}\}$ and their combination with $\{E\vert(0, 0, 1)\}$. $\{E\vert 0\}$ and $\{\sigma_h\vert 0\}$ both are unit 2×2 matrices in the spin space hence will not introduce any spin degeneracy, while by selecting basis as spin polarization along y, neither $\{C_{2x}\vert\boldsymbol{\tau}\}$ nor $\{\sigma_{vy}\vert\boldsymbol{\tau}\}$ will reverse the spin polarization. As the consequence, one would expect spin splitting along Z-R when SOC is included.

APPENDIX E: POWER OF k DEPENDENCE OF SPIN SPLITTING IN AFM MnF$_2$ WITH SOC

We have calculated the scaling of the spin splitting with a wave vector from DFT calculation: Nearby Γ (progressing along Γ-M), the splitting between the $V1$ and $V2$ bands shows a quadratic relation to the wave vector as $\boldsymbol{k}^\eta$ with a numerically fitted value of $\eta = 1.98$, while nearby Z (progressing along Z-R), such splitting shows a linear relation as $\boldsymbol{k}^\eta$ with numerical $\eta = 0.98$; the same quadratic and linear relations also hold for the splitting between $V3$ and $V4$ (see Table IV).

APPENDIX F: EFFECTIVE TWO-BAND MODEL HAMILTONIAN AT SPECIFIC k POINTS IN AFM MnF$_2$

In AFM MnF$_2$, one can define two spin-related AFM local atomic basis states [24] with one spin-up state localized mostly on Mn1 at $(0, 0, 0)$ and one spin-down state mostly localized on Mn2 at $(1/2, 1/2, 1/2)$. The AFM ordering is thus embedded in the inequivalence distribution on Mn1 and Mn2 of the spin-related basis. The effective two-band model Hamiltonian at specific k points can then be determined by the constrains imposed by the symmetries of the group of wave vector on the basis.

1. Effective model at Γ

At the Γ point, the group of wave vectors inherits all the symmetries that the AFM magnetic space group has. Upon applying the symmetries (only symmetry generators are needed) on the AFM basis one can find the representations and transformation properties of the Pauli matrix $\boldsymbol{\sigma}$ and tensor operator $\boldsymbol{k}$.

(1) When the SOC is ignored, the spin orientation is enforced to align along the magnetization direction, i.e. the, z axis. The corresponding magnetic space group is $P4_2'/mn'm$, which can be generated by three unitary symmetries $\{C_{2a}\vert 0\}$, $\{C_{2b}\vert 0\}$, $\{I\vert 0\}$ and one antiunitary symmetry $\theta\{C_{2x}\vert\boldsymbol{\tau}\}$. Table V lists the transformation properties of the Pauli matrix $\boldsymbol{\sigma}$ and tensor operator $\boldsymbol{k}$ under these symmetry operations; the only possible invariant spin splitting term that could exist in the Hamiltonian is $\sigma_z k_x k_y$, indicating quadratic dependence of spin splitting to displacement in $\boldsymbol{k}$ along the diagonal Γ-M direction, and spin degeneracy along the Γ-X direction in agreement with our DFT results seen in Fig. 2(b).

(2) When including SOC, the corresponding magnetic space group becomes $P4_2'/mnm'$, which can be generated by three unitary symmetries $\{C_{2x}\vert\boldsymbol{\tau}\}$, $\{C_{2y}\vert\boldsymbol{\tau}\}$, $\{I\vert 0\}$ and one antiunitary symmetry $\theta\{C_{2a}\vert 0\}$. The transformation properties of the Pauli matrix $\boldsymbol{\sigma}$ and tensor operator $\boldsymbol{k}$ are listed in Table VI.

We see from Table VI that the only possible invariant spin splitting term up to second order in $\boldsymbol{k}$ is $\sigma_z k_x k_y$, indicating quadratic dependence of spin splitting on variations in $\boldsymbol{k}$ along the diagonal Γ-M direction when SOC is included [see the DFT results in Fig. 1(c)]. The effective Hamiltonian term $\sigma_z k_x k_y$ also captures the four-quadrant pattern of the out-of-plane spin polarization as $k_x k_y$ having opposite signs in first and third quadrants and in second and fourth quadrants as seen in Fig. 3.

2. Effective model at Λ

(1) When SOC is excluded, the spin splitting term takes exactly the form as at Γ, $\sigma_z k_x k_y$, so there is no spin splitting along Λ-W and quadratic spin splitting along Λ-V.

(2) When SOC is included, from Table VII, the effective spin splitting terms are linear combinations of $H_\Lambda = A\sigma_z k_x k_y + B(\sigma_x k_y + \sigma_y k_x)$; here A and B are real coefficients. One would then also expect quadratic dependence along the diagonal Λ-V direction from the first term and linear dependence along the Λ-W direction from the second term. Also, the four quadrants pattern and Dresselhaus-like spin

TABLE VII. The transformation properties of symmetrized matrix and irreducible tensor under symmetry operations of the little point group at Λ with SOC.

Symmetrized matrix	Irreducible tensor	$\{\sigma_{vx}\vert\boldsymbol{\tau}\}$	$\{\sigma_{vy}\vert\boldsymbol{\tau}\}$	$\theta\{C_{2a}\vert 0\}$
σ_0	$C, k_x^2 + k_y^2, k_z^2$	1	1	1
σ_z	$k_x k_y$	-1	-1	1
(σ_x, σ_y)	(k_y, k_x)	$\begin{bmatrix} 1 & 0 \\ 0 & -1 \end{bmatrix}$	$\begin{bmatrix} -1 & 0 \\ 0 & 1 \end{bmatrix}$	$\begin{bmatrix} 0 & -1 \\ -1 & 0 \end{bmatrix}$

TABLE VIII. The transformation properties of symmetrized matrix and irreducible tensor under symmetry operations of the little point group at Z with SOC.

Symmetrized matrix	Irreducible tensor	$\{C_{2x}\vert\boldsymbol{\tau}\}$	$\{C_{2y}\vert\boldsymbol{\tau}\}$	$\{I\vert 0\}$	$\theta\{C_{2a}\vert 0\}$
σ_0	$C, k_x^2 + k_y^2, k_z^2$	1	1	1	1
σ_z	$k_x k_y$	-1	-1	1	1
$(\sigma_x,\ \sigma_y)$	$(k_y, -k_x)$	$\begin{bmatrix} -1 & 0 \\ 0 & 1 \end{bmatrix}$	$\begin{bmatrix} 1 & 0 \\ 0 & -1 \end{bmatrix}$	$\begin{bmatrix} -1 & 0 \\ 0 & -1 \end{bmatrix}$	$\begin{bmatrix} 0 & 1 \\ 1 & 0 \end{bmatrix}$

texture can be explicitly captured by the effective model Hamiltonian; the first term contributes to the four-quadrant pattern with out-of-plane spin polarization, where $k_x k_y$ takes opposite sign in first ($k_x > 0, k_y > 0$) and third ($k_x < 0, k_y < 0$) quadrants relative to the second ($k_x < 0, k_y > 0$) and fourth ($k_x > 0, k_y < 0$) quadrants. The second term resembles in analytical form the conventional Dresselhaus term and contributes the in-plane Dresselhaus spin texture. One should note that it is the distribution of the spin-related basis on two Mn that provides nonvanishing in-plane spin texture. If the spin-up and spin-down basis is localized completely on Mn1 and Mn2, the in-plane spin texture would vanish and there would be no Dresselhaus spin texture at all. Larger mixing between the two local Mn atoms of the spin basis will lead to a stronger in-plane spin polarization.

3. Effective model at Z

(1) When SOC is excluded, the spin splitting term takes exactly the form as at Γ, $\sigma_z k_x k_y$ and gives rise to zero spin splitting along Z-R, and quadratic-in-k spin splitting along Z-A [see the DFT band structure in Fig. 2(b)].

(2) When SOC is included, from Table VIII, the spin splitting terms are linear combinations of $H_Z = A\sigma_z k_x k_y + B(\sigma_x k_y - \sigma_y k_x)$; here A and B are real coefficients. Once again, the spin splitting will have quadratic dependence along the diagonal Z-A direction and a four-quadrant out-of-plane spin polarization pattern from the first term, and linear dependence along the Z-R direction from the second term. Moreover, despite the fact that the second term resembles in form the conventional Rashba Hamiltonian [2], it will not create in-plane spin polarization (see Fig. 4). The vanishing spin polarization is the consequence of zero mixing between the two spin-related Bloch bases of Mn1 and Mn2 for the same spin, that are $\vert Mn_1, \uparrow\rangle$ and $\vert Mn_2, \uparrow\rangle$ (also $\vert Mn_1, \downarrow\rangle$ and $\vert Mn_2, \downarrow\rangle$), which form a pair of zero in-plane spin polarized but nonzero splitting states, $a\vert Mn_1, \uparrow\rangle + b\vert Mn_2, \downarrow\rangle$ and $a\vert Mn_1, \uparrow\rangle - b\vert Mn_2, \downarrow\rangle$ with a, b being the complex constant coefficients of the states satisfying the normalization condition $\vert a\vert^2 + \vert b\vert^2 = 1$. When $a = b$, the out-of-plane spin polarization also vanishes. The zero mixing between $\vert Mn_1, \uparrow\rangle$ and $\vert Mn_2, \uparrow\rangle$ (and between $\vert Mn_1, \downarrow\rangle$ and $\vert Mn_2, \downarrow\rangle$) is enforced by $\{\sigma_h\vert 0\}$ symmetry at Z, since $\vert Mn_1, \uparrow\rangle$ (and $\vert Mn_2, \downarrow\rangle$) takes opposite eigenvalue of $\{\sigma_h\vert 0\}$ symmetry to $\vert Mn_2, \uparrow\rangle$ (and $\vert Mn_1, \downarrow\rangle$). The same reason accounts for the zero in-plane spin polarization but nonzero splitting observed at R when SOC is included, as $\{\sigma_h\vert 0\}$ is also a symmetry of $\boldsymbol{k}$ at R and forbids mixing between $\vert Mn_1, \uparrow\rangle$ and $\vert Mn_2, \uparrow\rangle$ (and between $\vert Mn_1, \downarrow\rangle$ and $\vert Mn_2, \downarrow\rangle$). The surprising effect of spin splitting with vanishing spin polarization was also reported recently

in nonmagnetic crystals (e.g., bulk GaAs [60] and graphene [61]).

APPENDIX G: IN-PLANE SPIN TEXTURE IN MnF$_2$ ON THE k PLANES $k_z = 0$ AND $k_z = \pi/c$

Figure 4 shows the calculated spin textures of the $V1$ and $V2$ bands in MnF$_2$ on $\boldsymbol{k}$ planes $k_z = 0$ and $k_z = \pi/c$, where c is the lattice constant along (001). For the out-of-plane spin polarization, we find the same four-quadrant pattern as the one found on the $k_z = \pi/2c$ plane (shown in Fig. 3). While, in contrast to in-plane Dresselhaus spin texture observed on $k_z = \pi/2c$ plane, on the $\boldsymbol{k}$ planes $k_z = 0$ and $k_z = \pi/c$, there is no in-plane spin polarization.

APPENDIX H: SPIN SPLITTING INDUCED BY COOPERATIVE EFFECTS OF AFM AND SOC IN MnF$_2$

Allowing SOC in a NM model does not lead to any spin splitting since the θI symmetry is always preserved [see Fig. 5 (a)]. In contrast, introducing SOC to AFM leads to cooperative effects of AFM + SOC. For example, it creates additional spin splitting along certain $\boldsymbol{k}$ paths, e.g., the Z-R, R-A, and
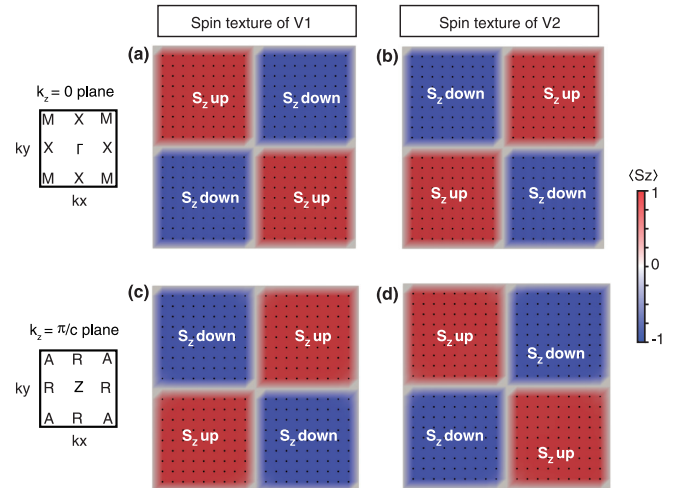
FIG. 4. Spin textures of the top two valence bands ($V1$ and $V2$) in AFM MnF$_2$ on two k_Z planes: (a) (b) $k_z = 0$ plane, and (d) and (e) $k_z = \pi/c$ plane. For each k_z plane, the labels of the high-symmetry $\boldsymbol{k}$ points are shown by a diagram on the left side of each horizonal panel. The in-plane spin polarizations are indicated by black arrows, while black dot means the in-plane polarization at this $\boldsymbol{k}$ is zero; the out-of-plane spin polarizations are mapped by colors from blue to red.
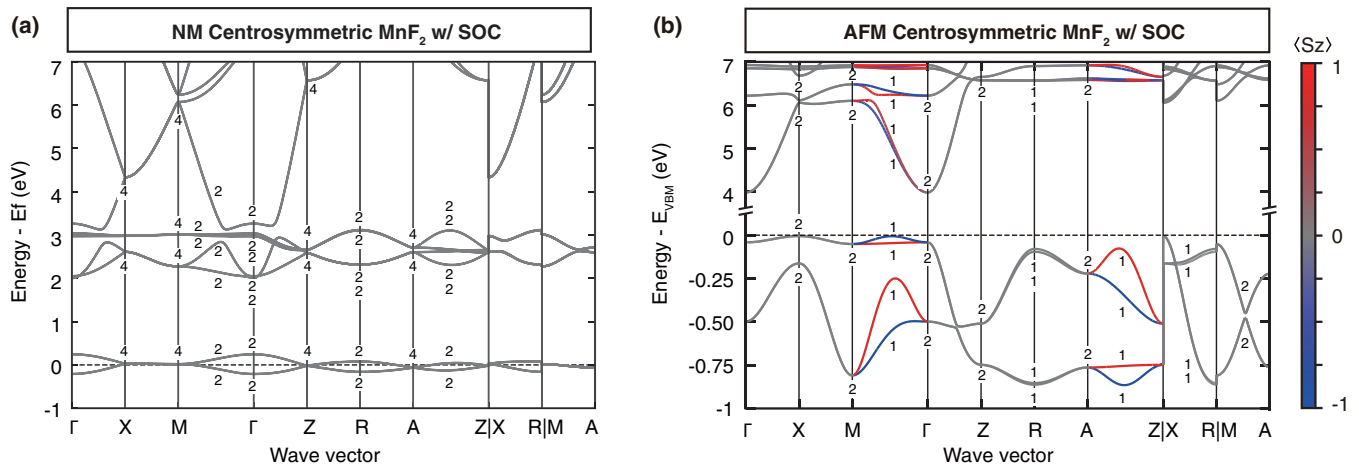
FIG. 5. DFT band structures of centrosymmetric MnF_2 in NM and AFM with SOC. In all cases we use the experimentally observed centrosymmetric tetragonal structure [37]: (a) NM with SOC; (b) AFM with SOC. Out-of-plane spin polarizations are mapped to color scales from blue to red. The integer numbers attached to bands are degeneracy factors.

X-R directions [see Fig. 5(b)]. This is because in the AFM phase described without SOC, the spin degeneracy along the *Z-R*, *R-A*, and *X-R* directions is guaranteed by the symmetry operations $\theta\{C_{2x}|\tau\}$, $\theta\{C_{2y}|\tau\}$, $\theta\{\sigma_{2x}|\tau\}$, and $\theta\{\sigma_{2y}|\tau\}$; adding SOC to pre-existing AFM couples the real-space rotations to spin operations and breaks all four antiunitary symmetries, leading therefore to spin splitting along these directions (see full details about how SOC induces spin splitting in preexisting AFM along *Z-R* in Appendix E). An interesting

fact is that we find spin splitting at the *R* point (which is TRIM) when adding SOC to the AFM phase. This manifests the breaking of time-reversal symmetry in the AFM phase. The lifting of spin degeneracy at the TRIM point and its connected **k** paths represents a cooperative effect of magnetism and SOC: neither AFM without SOC [Fig. 2(b)] nor SOC without AFM [Fig. 5(a)] shows spin splitting along these directions, but the coexistence of SOC and AFM leads to spin splitting.

[1] G. Dresselhaus, Phys. Rev. **100**, 580 (1955).

[2] E. Rashba and V. Sheka, Fiz. Tverd. Tela: Collected Papers **2**, 62 (1959).

[3] X. Zhang, Q. Liu, J.-W. Luo, A. J. Freeman, and A. Zunger, Nat. Phys. **10**, 387 (2014).

[4] L. D. Landau, J. S. Bell, M. J. Kearsley, L. P. Pitaevskii, E. M. Lifshitz, and J. B. Sykes, *Electrodynamics of Continuous Media* (Butterworth-Heinemann, Oxford, 1989), Vol. 8.

[5] S. A. Wolf, D. D. Awschalom, R. A. Buhrman, J. M. Daughton, S. v. Molnár, M. L. Roukes, A. Y. Chtchelkanova, and D. M. Treger, Science **294**, 1488 (2001).

[6] I. Žutić, J. Fabian, and S. D. Sarma, Rev. Mod. Phys. **76**, 323 (2004).

[7] A. Fert, Thin Solid Films **517**, 2 (2008).

[8] A. Manchon, H. C. Koo, J. Nitta, S. M. Frolov, and R. A. Duine, Nat. Mater. **14**, 871 (2015).

[9] F. Bailly, Phys. Status Solidi B **25**, 317 (1968).

[10] T. Taguchi and B. Ray, Prog. Cryst. Growth Charact. **6**, 103 (1983).

[11] D. West, Y. Y. Sun, H. Wang, J. Bang, and S. B. Zhang, Phys. Rev. B **86**, 121201(R) (2012).

[12] A. H. Edwards, A. C. Pineda, P. A. Schultz, M. G. Martin, A. P. Thompson, H. P. Hjalmarson, and C. J. Umrigar, Phys. Rev. B **73**, 045210 (2006).

[13] T. Jungwirth, X. Marti, P. Wadley, and J. Wunderlich, Nat. Nanotechnol. **11**, 231 (2016).

[14] A. H. MacDonald and M. Tsoi, Philos. Trans. R. Soc. Math. Phys. Eng. Sci. **369**, 3098 (2011).

[15] A. Manchon, J. Železný, I. M. Miron, T. Jungwirth, J. Sinova, A. Thiaville, K. Garello, and P. Gambardella, Rev. Mod. Phys. **91**, 035004 (2019).

[16] V. Baltz, A. Manchon, M. Tsoi, T. Moriyama, T. Ono, and Y. Tserkovnyak, Rev. Mod. Phys. **90**, 015005 (2018).

[17] S.-J. Hu and X. Hu, J. Phys. Chem. C **114**, 11614 (2010).

[18] G. Y. Gao and K.-L. Yao, Appl. Phys. Lett. **103**, 232409 (2013).

[19] S.-J. Gong, C. Gong, Y.-Y. Sun, W.-Y. Tong, C.-G. Duan, J.-H. Chu, and X. Zhang, Proc. Natl. Acad. Sci. U.S.A. **115**, 8511 (2018).

[20] K. Yamauchi, P. Barone, and S. Picozzi, Phys. Rev. B **100**, 245115 (2019).

[21] R. Ramazashvili, Phys. Rev. Lett. **101**, 137202 (2008).

[22] E. J. Rozbicki, J. F. Annett, J.-R. Souquet, and A. P. Mackenzie, J. Phys.: Condens. Matter **23**, 094201 (2011).

[23] S. I. Pekar and E. I. Rashba, Zh. Eksp. Teor. Fiz. **47**, 1927 (1964) [Sov. Phys. JETP **20**, 1295 (1965)].

[24] P. Tang, Q. Zhou, G. Xu, and S.-C. Zhang, Nat. Phys. **12**, 1100 (2016).

[25] C. Bradley and A. Cracknell, *The Mathematical Theory of Symmetry in Solids: Representation Theory for Point Groups and Space Groups* (Oxford University Press Inc., 2010), Chap. 7.

[26] S. V. Gallego, J. M. Perez-Mato, L. Elcoro, E. S. Tasci, R. M. Hanson, K. Momma, M. I. Aroyo, and G. Madariaga, J. Appl. Crystallogr. **49**, 1750 (2016).

[27] R. A. Erickson, Phys. Rev. **90**, 779 (1953).

[28] J. Rodriguez-Carvajal, M. Fernandez-Diaz, and J. Martinez, J. Phys.: Condens. Matter **3**, 3215 (1991).

[29] M.-R. Li, U. Adem, S. R. C. McMitchell, Z. Xu, C. I. Thomas, J. E. Warren, D. V. Giap, H. Niu, X. Wan, R. G. Palgrave, F. Schiffmann, F. Cora, B. Slater, T. L. Burnett, M. G. Cain, A. M. Abakumov, G. van Tendeloo, M. F. Thomas, M. J. Rosseinsky, and J. B. Claridge, J. Am. Chem. Soc. **134**, 3737 (2012).

[30] I. Tomeno, H. N. Fuke, H. Iwasaki, M. Sahashi, and Y. Tsunoda, J. Appl. Phys. **86**, 3853 (1999).

[31] P. Wadley, V. Hills, M. R. Shahedkhah, K. W. Edmonds, R. P. Campion, V. Novák, B. Ouladdiaf, D. Khalyavin, S. Langridge, V. Saidl, P. Nemec et al., Sci. Rep. **5**, 17079 (2015).

[32] E. Ressouche, N. Kernavanois, L.-P. Regnault, and J.-Y. Henry, Phys. B (Amsterdam, Neth.) **385-386**, 394 (2006).

[33] A. A. Belik et al., Chem. Mater. **18**, 798 (2006).

[34] S. Hayami, Y. Yanagi, and H. Kusunose, J. Phys. Soc. Jpn. **88**, 123702 (2019).

[35] M. Naka, S. Hayami, H. Kusunose, Y. Yanagi, Y. Motome, and H. Seo, Nat. Commun. **10**, 4305 (2019).

[36] J. W. Stout and H. E. Adams, J. Am. Chem. Soc. **64**, 1535 (1942).

[37] W. H. Baur and A. A. Khan, Acta Crystallogr., Sect. B: Struct. Crystallogr. Cryst. Chem. **27**, 2133 (1971).

[38] J. O. Dimmock and R. G. Wheeler, Phys. Rev. **127**, 391 (1962).

[39] J. P. Perdew, J. A. Chevary, S. H. Vosko, K. A. Jackson, M. R. Pederson, D. J. Singh, and C. Fiolhais, Phys. Rev. B **46**, 6671 (1992).

[40] J. Varignon, M. Bibes, and A. Zunger, Nat. Commun. **10**, 1658 (2019).

[41] G. Trimarchi, Z. Wang, and A. Zunger, Phys. Rev. B **97**, 035107 (2018).

[42] J. W. Stout, J. Chem. Phys. **31**, 709 (1959).

[43] K. Ishizaka, M. S. Bahramy, H. Murakawa, M. Sakano, T. Shimojima, T. Sonobe, K. Koizumi, S. Shin, H. Miyahara, A. Kimura, K. Miyamoto et al., Nat. Mater. **10**, 521 (2011).

[44] D. D. Sante, P. Barone, R. Bertacco, and S. Picozzi, Adv. Mater. **25**, 509 (2012).

[45] M. Liebmann, C. Rinaldi, D. Di Sante, J. Kellner, C. Pauly, R. N. Wang, J. E. Boschker, A. Giussani, S. Bertoli, M. Cantoni, L. Baldrati et al., Adv. Mater. **28**, 560 (2015).

[46] S. J. May, P. J. Ryan, J. L. Robertson, J.-W. Kim, T. S. Santos, E. Karapetrova, J. L. Zarestky, X. Zhai, S. G. E. te Velthuis, J. N. Eckstein, S. D. Bader, and A. Bhattacharya, Nat. Mater. **8**, 892 (2009).

[47] J. Železný, H. Gao, K. Výborný, J. Zemen, J. Mašek, A. Manchon, J. Wunderlich, J. Sinova, and T. Jungwirth, Phys. Rev. Lett. **113**, 157201 (2014).

[48] P. Wadley, B. Howells, J. Železný, C. Andrews, V. Hills, R. P. Campion, V. Novák, K. Olejník, F. Maccherozzi, S. S. Dhesi, S. Y. Martin et al., Science **351**, 587 (2016).

[49] Y. Tazaki, Y. Kageyama, H. Hayashi, T. Harumoto, T. Gao, J. Shi, and K. Ando, arXiv:2004.09165.

[50] S. Geprägs, M. Opel, J. Fischer, O. Gomonay, P. Schwenke, M. Althammer, H. Huebl, and R. Gross, J. Appl. Phys. **127**, 243902 (2020).

[51] P. Högl, T. Frank, K. Zollner, D. Kochan, M. Gmitra, and J. Fabian, Phys. Rev. Lett. **124**, 136403 (2020).

[52] J. Železný, Y. Zhang, C. Felser, and B. Yan, Phys. Rev. Lett. **119**, 187204 (2017).

[53] H. Chen, Q. Niu, and A. H. MacDonald, Phys. Rev. Lett. **112**, 017205 (2014).

[54] M. T. Suzuki, T. Koretsune, M. Ochi, and R. Arita, Phys. Rev. B **95**, 094406 (2017).

[55] L. Šmejkal, R. González-Hernández, T. Jungwirth, and J. Sinova, arXiv:1901.00445.

[56] Z. Feng, X. Zhou, L. Šmejkal, L. Wu, Z. Zhu, H. Guo, R. González-Hernández, X. Wang, H. Yan, P. Qin, X. Zhang et al., arXiv:2002.08712.

[57] H. J. Monkhorst and J. D. Pack, Phys. Rev. B **13**, 5188 (1976).

[58] A. I. Liechtenstein, V. I. Anisimov, and J. Zaanen, Phys. Rev. B **52**, R5467(R) (1995).

[59] S. Steiner, S. Khmelevskyi, M. Marsmann, and G. Kresse, Phys. Rev. B **93**, 224425 (2016).

[60] K. Liu, W. Luo, J. Ji, P. Barone, S. Picozzi, and H. Xiang, Nat. Commun. **10**, 5144 (2019).

[61] E. I. Rashba, Phys. Rev. B **79**, 161409(R) (2009).